



# The Role of the Counterbody's Oxide on the Wear Behavior of HSS and Hi-Cr

O. A. Zambrano<sup>1</sup> · K. F. Gallardo<sup>1</sup> · D. M. Polania<sup>1</sup> · S. A. Rodríguez<sup>1</sup> · J. J. Coronado<sup>1</sup>

Received: 8 September 2017 / Accepted: 10 November 2017 / Published online: 17 November 2017  
© Springer Science+Business Media, LLC, part of Springer Nature 2017

## Abstract

The wear behavior of two high-speed steels and a high-chromium cast iron with cryogenic treatments was evaluated using a pin-on-disc configuration. An ASTM A36 steel disc, oxidized previously in a furnace at 950 °C, was used as a counterbody with the goal of developing an accurate representation of the industrial calamine formed on the surface of steels under industrial conditions. This is a new perspective to evaluate the real contribution of the normal load, sliding velocity and heat treatments on the wear phenomena of hot rolls. Optical microscopy, scanning electron microscopy and X-ray diffraction were used to correlate the wear rate, friction coefficient and wear mechanisms to the microstructure, hardness and types of oxides that formed on the counterbody. Experimental results showed a complex relation between the normal load, the sliding velocity and the interaction with counterbody, which establishes the wear rates and friction coefficients.

**Keywords** Wear · High-speed steel · High-chromium cast iron · Iron oxides

## 1 Introduction

The wear of hot rolling mills is one of the main factors affecting the hot rolling process. For instance, achieving required sheet specifications and better performance in terms of tons produced per unit time is directly affected by wear phenomena. Different studies have been used to evaluate the wear of hot rolls in the steelmaking industry by employing configurations such as disc-on-disc and block-on-disc to represent the sliding component of real hot rolls and study load effect [1–3]. Pin-on-disc, pin-on-abrasive paper and block-on-rubber wheel have been used to analyze abrasive wear behavior by different authors [4–8]. In addition, the influence of oxides on the tribological behavior of these materials has been studied using pin-on-disc [2, 6, 9], disc-on-disc [10] and block-on-ring [11] configurations.

High-chromium cast irons (Hi-Cr) and high-speed steels (HSS) have been used broadly to produce hot rolling mills for the steel-maker industry due to their good wear properties. For instance, Doğan et al. [12] evaluated the wear resistance of different Hi-Cr cast irons (15–26% Cr) using

the pin-on-ring configuration. They found that the austenite matrix exhibited a higher wear resistance than pearlitic and bainitic matrices due to the strain hardening capacity, which increases the superficial hardness and decreases the carbide fracture phenomenon. However, when is only evaluated the wear behavior of Hi-Cr cast iron with different retained austenite contents using pin-on-abrasive paper, Tabrett et al. [13] showed that using cryogenic treatments caused a decrease in the retained austenite, which increase the wear resistance up to 30%. These results are consistent with those of Liu et al. [14], who obtained an increase in the wear resistance by decreasing the retained austenite using cryogenic treatments in the pin-on-abrasive paper configuration.

HSS have been used extensively as the initial mills in finishing trains [15] due to their good wear resistance [16]. These types of HSS are member of the Fe–C–Cr–W–Mo–V system, which is generally used for fabricating hot rolling mills and for mill trituration in the mining industry due to its high wear resistance. The metallurgical design of these alloys is based on the M2 steel composition, with the main changes being higher carbon and vanadium contents. Companies develop particular compositions according to the market that they serve. However, the chemical compositions are always in the range of (wt%) 1.5–2.6% C, < 5% W, < 5% Mo, 3–7% Cr, 4–8% V and in some cases < 5% Co [17]. The

✉ J. J. Coronado  
john.coronado@correounivalle.edu.co

<sup>1</sup> Research Group of Fatigue and Surfaces, Mechanical Engineering School, Universidad del Valle, Cali, Colombia

HSS wear properties are mainly attributed to a net of high hardness carbides supported by a hard-martensitic matrix. Obviously, the type and morphology of the carbides and the microstructural features of the matrix drastically influence the wear behavior [18]. Recently, Penagos et al. [8] studied the effect of microstructure refinement for a Hi-Cr cast iron and found that high microstructure refinement produces a drastic decrease in the wear resistance. These contra-intuitive results are primarily because the  $M_7C_3$  carbides in the finer microstructure promote subsurface cracking, which produces a high mass loss. Other factors, such as the type and morphology of the carbides, determine the wear behavior. This was verified by Nilsson and Olsson [19], who studied HSS, Cr cast iron and a chill cast iron and found that the wear resistance of the HSS was higher than that of the Cr cast irons, mainly due to the type of primary carbides in the microstructure. Similar investigations conducted by Xavier et al. [15], who studied the wear of hot rolls in a pin-on-disc configuration and examined three materials commonly used for this application: Hi-Cr, a mottled cast iron (MCI) and an HSS. The abrasive used was alumina paper (2200 HV), which is harder than the  $M_{23}C_6$  (1200 HV),  $M_6C$  (1500 HV),  $M_7C_3$  (1800 HV), and  $M_2C$  (2000 HV), but softer than the MC carbides (3000 HV). The results showed that HSS exhibited a higher wear resistance than the Hi-Cr and IC irons, primarily due to the high content of the vanadium carbides (MC). However, it is important to note that the increase in the friction coefficient is directly related to the increase in the MC fraction [17].

It is also important to take into account the effect of the counterbody in the tribological pair. During the hot rolling process, steel is usually processed in the temperature range between 900 and 1200 °C. At these temperatures, the steel slab generates, as a first approximation, three iron oxide layers on the surface. The inner oxide is wüstite (FeO), the intermediate oxide is cubic magnetite ( $Fe_3O_4$ ), and the external oxide is rhombohedral hematite ( $\alpha-Fe_2O_3$ ). Recently, Zambrano et al. [20] showed that the internal, intermediate and external oxide layers produced in a low carbon steel at high temperatures are also composed of the three main oxides [wüstite (FeO), magnetite ( $Fe_3O_4$ ) and hematite ( $\alpha-Fe_2O_3$ )]. These three iron oxide layers have different hardnesses. Wüstite (FeO) has the lowest hardness (~ 317 HV) and has good lubricity at high temperatures, which decreases the wear and the friction coefficient. Magnetite ( $Fe_3O_4$ ) has

an intermediate hardness (~ 465 HV) and is also considered to be a solid lubricant at high temperatures, whereas hematite ( $\alpha-Fe_2O_3$ ) has the highest hardness (~ 975 HV), which promotes abrasive wear [20]. For the aforementioned features of the counterbody, it is important to take into account the effect of these oxides on the tribological pair to achieve a better understanding of the involved phenomena.

Previous studies have examined the wear behavior of HSS and Hi-Cr alloys using standard heat treatments and counterbodies. Presently, few investigations have examined the effect of cryogenic treatments on the tribological response (wear, friction coefficients, wear surfaces, etc.) and/or other counterbodies, which may be more applicable to the industrial conditions in the steelmaking industry and may more accurately replicate the wear behavior. This is a new assessment of the contribution of the normal load, sliding velocity and heat treatments on very commercial hot roll materials.

## 2 Experimental Procedure

### 2.1 Materials

The chemical composition of the two high-speed steels and the high-chromium cast iron were determined using an optical emission ARL 3460 Advantage spectrometer, as shown in Table 1.

### 2.2 Heat Treatments

#### 2.2.1 High-Speed Steel 1 (HSS1)

The thermal treatment used for the HSS1 is described as follows: a total annealing treatment was performed, which consists of an initial heating above the austenite transformation temperature. Generally, this temperature varies between 810 and 850 °C for high-speed steels. The samples were introduced to mineral carbon to avoid decarburization problems and then heated to 850 °C for 2 h at a rate of 15 °C/min to avoid cracking from thermal stresses during phase transformation. The samples were cooled in a furnace to room temperature. Then, the samples were austenitized at 1200 °C for 0.5 h and quenched in oil. Finally, three tempering treatments were performed consecutively at 550 °C for 2 h for each one.

**Table 1** Composition (wt%) of the high-speed steels and the high-chromium cast iron

| Alloy | C    | W    | Elements wt% |       |      |      |      |
|-------|------|------|--------------|-------|------|------|------|
|       |      |      | Mo           | Cr    | V    | Ni   | Nb   |
| HSS1  | 1.97 | 2.15 | 2.06         | 6.59  | 4.74 | 0.83 | 0.02 |
| HSS2  | 2.41 | 2.29 | 2.28         | 6.94  | 5.53 | 0.76 | 0.09 |
| Hi-Cr | 2.50 | –    | 1.27         | 16.27 | 0.21 | 1.16 | 0.01 |

### 2.2.2 High-Speed Steel 2 (HSS2)

HSS2 was quenched in oil, tempered and treated cryogenically. Pins for the abrasion test were obtained with dimensions of  $\phi 3$  mm  $\times$  15 mm length using electro-discharge machining, with additional samples cut for metallographic analysis. The hardness and microstructural characterization will be discussed later.

### 2.2.3 High-Chromium Cast Iron 1 (CT1)

The High-Cr cast iron samples in the as-cast condition were introduced into a bath of liquid nitrogen ( $-196.6$  °C) for a period of 3 h.

### 2.2.4 High-Chromium Cast Iron 2 (CT2)

Cryogenic treatment consists of austenitizing the samples at 1050 °C for 2 h at a rate of 15 °C/min in an electrical furnace, then, air quenching was performed until the samples reached room temperature, afterward, the samples were submerged in a bath of liquid nitrogen for 3 h. Finally, a double tempering treatment was performed at 500 °C for 3 h at a rate of 15 °C/min. The samples were cooled inside the furnace in both cases.

## 2.3 Hardness Test

Macrohardness testing was performed on the heat-treated samples using a Rockwell C scale tester. Microhardness testing was performed on the heat-treated samples using a Vickers indenter at 50 gf for 10 s. The test errors were determined with 95% confidence.

## 2.4 Tribological Test

Wear tests were performed on a pin-on-disc tribometer Microtest MT/10/SCM. Sliding wear tests were carried out using HSS and Hi-Cr cast iron pins (3 mm of diameter with a flat-ended) against an ASTM A36 steel disc previously oxidized. The applied parameters evaluated were a constant tangential speed of 0.2 m/s and 0.6 m/s, normal loads of 5 and 10 N and a total sliding distance of 600 m. Three repetitions were performed for each condition, and the test errors were determined with 95% confidence. For each pin, a superficial homogenization stage was produced using alumina 600 grit abrasive paper with a normal load of 5 N. This procedure was repeated before each wear test. Finally, the mass losses of the pins were measured using a high-resolution analytical scale brand Rabwad MXA2 with 0.000001 g (1  $\mu$ g) resolution.

The progress of the friction coefficient with the sliding distance for different normal loads and alloys used were

recorded. The friction coefficient values discussed during the text are referred to the stable friction coefficient.

### 2.4.1 Counterbody Preparation

The first step in counterbody preparation consists of obtaining discs with radii of 35 mm from a sheet of ASTM A36 steel with a thickness of 3 mm via laser cutting. The ASTM A36 disc samples were cleaned using a sandblasting equipment (Campbell Hausfeld AT125102) for a uniform surface and to promote anchorage for the subsequent oxidation process. For the sandblasting process, the sand size particles were less than 2 mm, which was guaranteed using a number 10 (ASTM E 11-95) sieve. The air pressure employed was 5.5 bars. The Ra roughness on the disc surface obtained was  $5.62 \pm 0.16$   $\mu$ m.

Afterward, the discs were cleaned using ethanol and placed in a low vacuum chamber at  $-0.6$  bars gage to avoid oxidation or further surface modification. Then, the discs were submitted to an oxidation process in air at a heating rate of 15 °C/min until reaching an oxidation temperature of 950 °C. The samples were held at this temperature for 30 min and cooled inside the furnace to avoid or reduce thermal stresses that can cause cracking or detachment of the oxide layers. The oxide layer had a final roughness of  $3.61 \pm 0.24$   $\mu$ m of Ra, a thickness of  $733.82 \pm 70.17$   $\mu$ m and an HV<sub>50gf</sub> hardness on the external layer of  $975.5 \pm 62.7$ . The oxidized surface was then analyzed by SEM, as shown in Fig. 1. The micrograph displays a fine oxide morphology with a granular form. The low roughness dispersion of the oxidized disc permits its use as a stable counterbody for subsequent wear tests. This counterbody has also been used satisfactorily in hot wear conditions for mottled cast iron [6]. This reinforces its potential as a more approximate counterbody to the study materials for the hot rolling process.

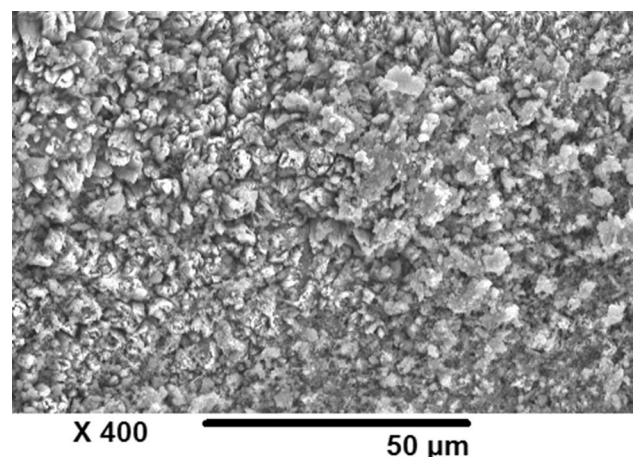


**Fig. 1** Oxide morphology obtained by SEM for the ASTM A36 disc oxidized at 900 °C by 30 min

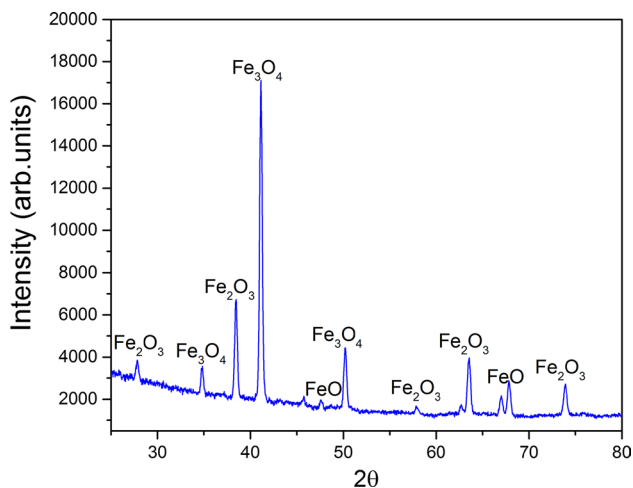


**Fig. 2** XRD patterns for the outer oxide layer of the oxidized (900 °C for 30 min) low carbon steel surface

**Table 2** Weight percentages of the oxides in the outer layers for the oxidized (900 °C for 30 min) low carbon steel

| Oxide                                       | wt%   |
|---|-------|
| Magnetite (Fe <sub>3</sub> O <sub>4</sub> ) | 68.35 |
| Wüstite (FeO)                               | 16.69 |
| Hematite (Fe <sub>2</sub> O <sub>3</sub> )  | 14.96 |

However, when the sample oxidized is cut transversally, it can be identifying three layers. The external layer is composed mainly of hematite ( $\alpha$ -Fe<sub>2</sub>O<sub>3</sub>), the intermediate layer is mainly magnetite (Fe<sub>3</sub>O<sub>4</sub>), and the inner oxide layer is mainly wüstite (FeO). A detailed characterization of these three iron oxides obtained after an oxidation treatment using XRD, Raman spectroscopy, SEM and nanoindentation can be found in [20] for reference.

The oxide layer of the ASTM A36 steel oxidized in the present conditions (900 °C for 30 min) was analyzed via XRD to determine the type and percentage of the oxides on the outer surface (the surface in contact with the pin). The XRD data were obtained at room temperature using a PANalytical diffractometer in the grazing incidence diffraction configuration and Co  $\alpha$  radiation (45 kV, 40 mA). The scan was collected with a grazing incidence angle of 1.5°. The samples were scanned over  $2\theta$  angles between 10° and 100° with a  $2\theta$  scan step of 0.02°. The weight percentages of the phases were calculated using the Rietveld method [21], and refinements were processed using the GSAS software [22]. The XRD results from the oxides on the outer surface are shown in Fig. 2 and Table 2.

The results obtained from the outer layer indicate that the oxide is composed of a mixture of different iron oxides: magnetite (Fe<sub>3</sub>O<sub>4</sub>), wüstite (FeO) and hematite (Fe<sub>2</sub>O<sub>3</sub>). These results are consistent with the results reported by Zambrano et al. [20]. However, the oxide proportions differ

for the outer layer. In this study, a higher proportion of magnetite was found, which may be explained by differences in the oxidation temperatures and times compared to the work of Zambrano et al.

## 3 Results

### 3.1 Microstructures

#### 3.1.1 HSS1

After cooling the HSS1, the initial microstructure consisted of primary MC and M<sub>6</sub>C carbides dispersed in a martensitic (M) matrix with some retained austenite (A). This microstructure was consistent with the results of Silva [23], who found that at temperatures between 900 and 1100 °C, all the M<sub>23</sub>C<sub>6</sub> carbides are dissolved, and at temperatures above 1160 °C, the M<sub>6</sub>C and M<sub>2</sub>C carbides start to dissolve. However, these are completely dissolved only if the temperature is greater than the solidification temperature. Additionally, over this last range of temperatures, the MC carbides cannot be dissolved.

Three tempering treatments were performed to ensure (i) a drastic decrease in the austenite content, which in the quenched condition, may be as high as 30%, and (ii) assure the highest secondary hardness possible, which usually occurs for tempering temperatures of 550 °C. Figure 3a shows a microstructure with different phases; tempered martensite (dark area), retained austenite with needles of martensite, MC carbides and a eutectic phase ( $\gamma + M_xC_y$ ) that corresponds to the white area. Figure 3b shows that the eutectic phase is surrounded by retained austenite. It is also interesting to point out that even and after three tempering treatments, the retained austenite phase is still unsuppressed.

#### 3.1.2 HSS2

Figure 4 shows the HSS2 microstructure, which contain MC carbides inside the grains, which are in a tempered martensite matrix. No austenite was observed, which is in agreement with other authors describing similar steels, who found that after deep cryogenic treatments, the amount of retained austenite was negligible [24].

#### 3.1.3 CT1

The initial microstructure (without cryogenic treatment) of CT1 is shown in Fig. 5a and is composed of austenite with M<sub>23</sub>C<sub>6</sub> secondary carbides precipitated inside the grains related to the eutectic phase ( $\gamma + M_{23}C_6$ ), which includes primary chromium carbides (M<sub>7</sub>C<sub>3</sub>) with eutectic cells composed of austenite and secondary molybdenum carbides

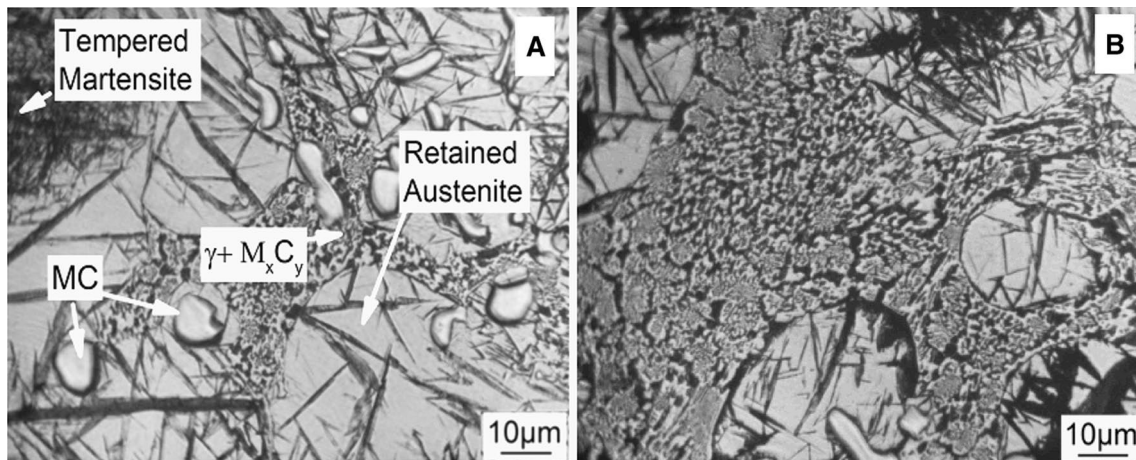


**Fig. 3** Microstructures of HSS1: **a** different phases, and **b**  $\gamma + M_xC_y$  eutectic phase

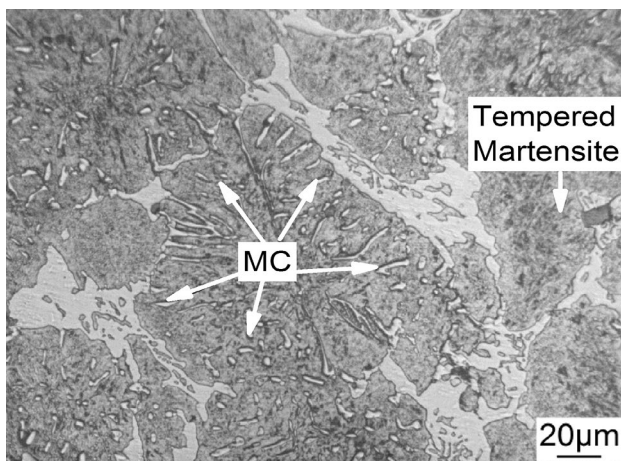


**Fig. 4** Microstructure of HSS2

( $M_2C$ ). The low hardness was obtained (see Sect. 3.2.2), and the vast amount of austenite is undesirable for hot rolling applications. For this reason, a cryogenic treatment was employed to increase the hardness and decrease the austenite content. The microstructure after 3 h of cryogenic treatment is shown in Fig. 5b. This microstructure is characterized by primary  $M_7C_3$  carbides, secondary precipitated  $M_{23}C_6$  carbides inside the grains with transformed austenite into martensite. It is evident that the austenite content for this treatment is lower than in the original microstructure (Fig. 5a). The decrease in the austenite content as a result of the cryogenic treatment is mainly due to the approximation of the finish martensite temperature ( $M_f$ ), which is below room temperature. However, not all the austenite is transformed and some retained austenite should be present.

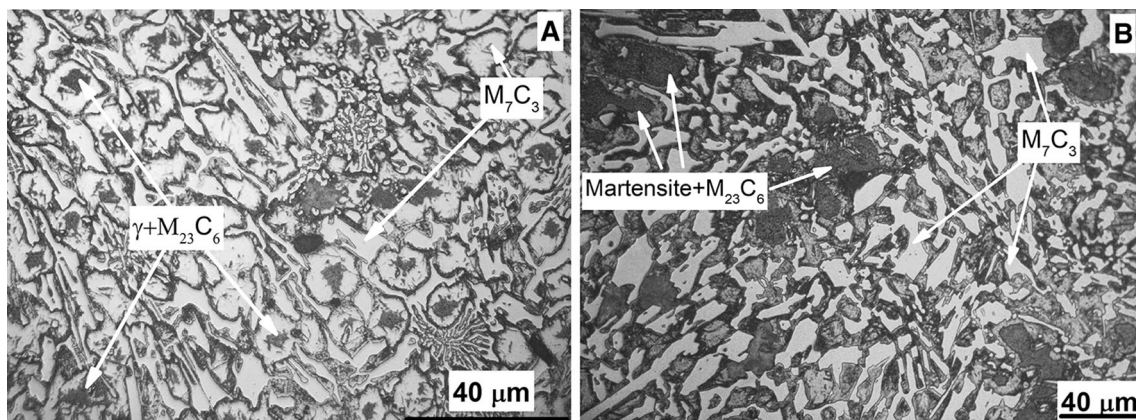


**Fig. 5** **a** Initial Hi-Cr cast iron microstructure (without any treatment), **b** microstructure after 3 h cryogenic treatment (CT1)

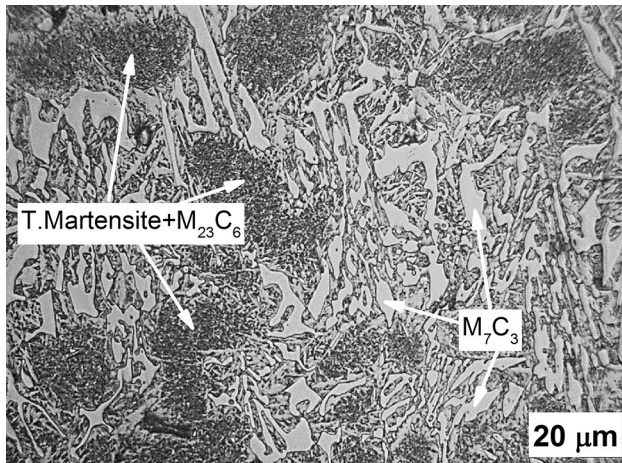


**Fig. 6** Hi-Cr cast iron microstructure obtained after austenitizing, quenching, cryogenic treatment and double tempering (CT2)

### 3.1.4 CT2

The microstructure for CT2 obtained after austenitizing, quenching, cryogenic treatment and double tempering is shown in Fig. 6. A tempered martensite matrix and chromium eutectic carbides  $M_7C_3$ , secondary  $M_{23}C_6$  carbides are present in the microstructure (the reader is refer to the work of Vitry et al. [18] and Molinari et al. [25] to compare the carbide morphology and identification). The secondary carbides precipitate during cooling and from the tempering treatment, enhancing the hardness and toughness [13, 26]. As mentioned, the cryogenic treatment promotes the transformation of retained austenite to martensite and increases the volume fraction of  $M_{23}C_6$  carbides and secondary carbides in the matrix [14]. These carbides were identified using scanning electron microscopy and EDS (see Sect. 4.2.2.1). Additionally, the tempering treatment also decreases the retained austenite, which has been reported by Da Silva [23], who described a high-chromium cast iron in which the austenite content decreased to  $< 0.5\%$  after three tempering treatments.

## 3.2 Hardness Test

### 3.2.1 HSS1

The macrohardness values for each thermal treatment performed on HSS1 are shown in Fig. 7. An increase in the hardness was observed after each tempering treatment due to the secondary precipitation and is present in most of tool steels [18]. Additionally, there is a relatively large dispersion of the hardness in the quenched condition, which is mainly due to the heterogeneity of the martensite and the retained austenite.

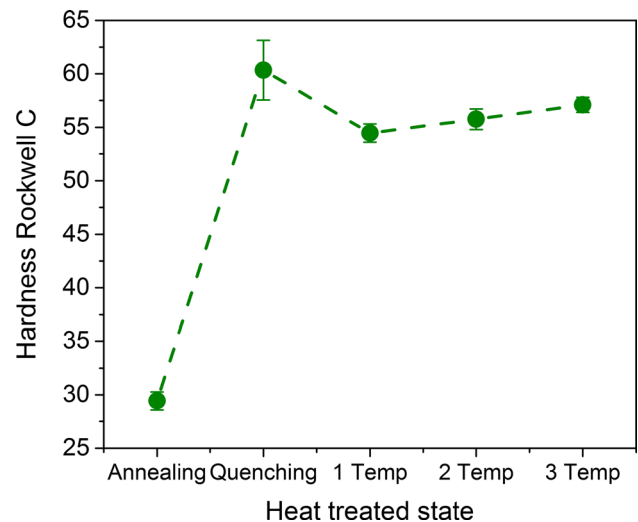


**Fig. 7** Rockwell C hardness as a function of heat treatment for the HSS1

Table 3 shows the microhardness of the different phases present in HSS1 after the heat treatments. The hardest phase was the MC carbide, which has a hardness above 2500 HV for both steels. These carbides exhibited hardness below the values ( $\sim 3200$  HV) reported by M. Nilsson [27]. This is due to the indenter not being able to specifically indent only the carbide and interacting with the matrix to some extent. The hardness of HSS1 is characterized by a hard phase of MC carbides, and a soft phase of tempered martensite, the eutectic phase and retained austenite.

### 3.2.2 HSS2

For HSS2, the initial macrohardness was determined to be  $HRC 54.08 \pm 0.29$ . The microhardness for each phase is shown in Table 4. HSS2 showed a greater difference between the hardest and softest phases than observed in HSS1.

### 3.2.3 Hi-Cr Cast Iron CT1 and CT2

The macrohardness and microhardness of the Hi-Cr cast iron before and after the cryogenic treatments are shown in Table 5. The increase in the hardness is evident for the cryogenic treated Hi-Cr cast iron. CT2 exhibited a greater increase in the hardness than CT1, which is due to the additional tempering treatments that promoted secondary precipitation hardening.

## 4 Wear Test

The wear behavior of the HSS and Hi-Cr using a pre-oxidized ASTM A36 disc as the counterbody is analyzed

**Table 3** HSS1 microhardness after the heat treatment

| Phases                              | Tempered martensite | Retained austenite ( $\gamma$ ) | Eutectic phase ( $\gamma + M_xC_y$ ) | MC carbide     |
|-------------------------------------|---------------------|---------------------------------|--------------------------------------|----------------|
| Microhardness (HV <sub>0.05</sub> ) | 808.4 ± 53.4        | 696.8 ± 44.2                    | 865.6 ± 97.7                         | 2584.5 ± 204.8 |

**Table 4** HSS2 microhardnesses

| Phases                              | Tempered martensite | Complex-carbide | MC carbide     |
|-------------------------------------|---------------------|-----------------|----------------|
| Microhardness (HV <sub>0.05</sub> ) | 724.0 ± 89.7        | 1634.2 ± 248.4  | 2623.4 ± 162.8 |

**Table 5** Microhardnesses of the Hi-Cr cast iron before and after the CT1 and CT2 heat treatments

| Thermal treatment                     | Macrohardness (HRC) | Microhardness (HV <sub>0.05</sub> ) |                                   |                          |
|---------------------------------------|---------------------|-------------------------------------|-----------------------------------|--------------------------|
|                                       |                     | Eutectic carbides                   | Retained austenite and martensite | Small precipitates zones |
| Without cryogenic treatment (initial) | 52.9 ± 1.14         | 1129.0 ± 34.0                       | 726.4 ± 65.0                      | 617.2 ± 69.0             |
| CT1                                   | 55.0 ± 0.50         | 1180.3 ± 45.0                       | 789.2 ± 15.0                      | 680.7 ± 45.0             |
| CT2                                   | 58.0 ± 2.50         | 1230.8 ± 14.0                       | 897.6 ± 80.0                      |                          |

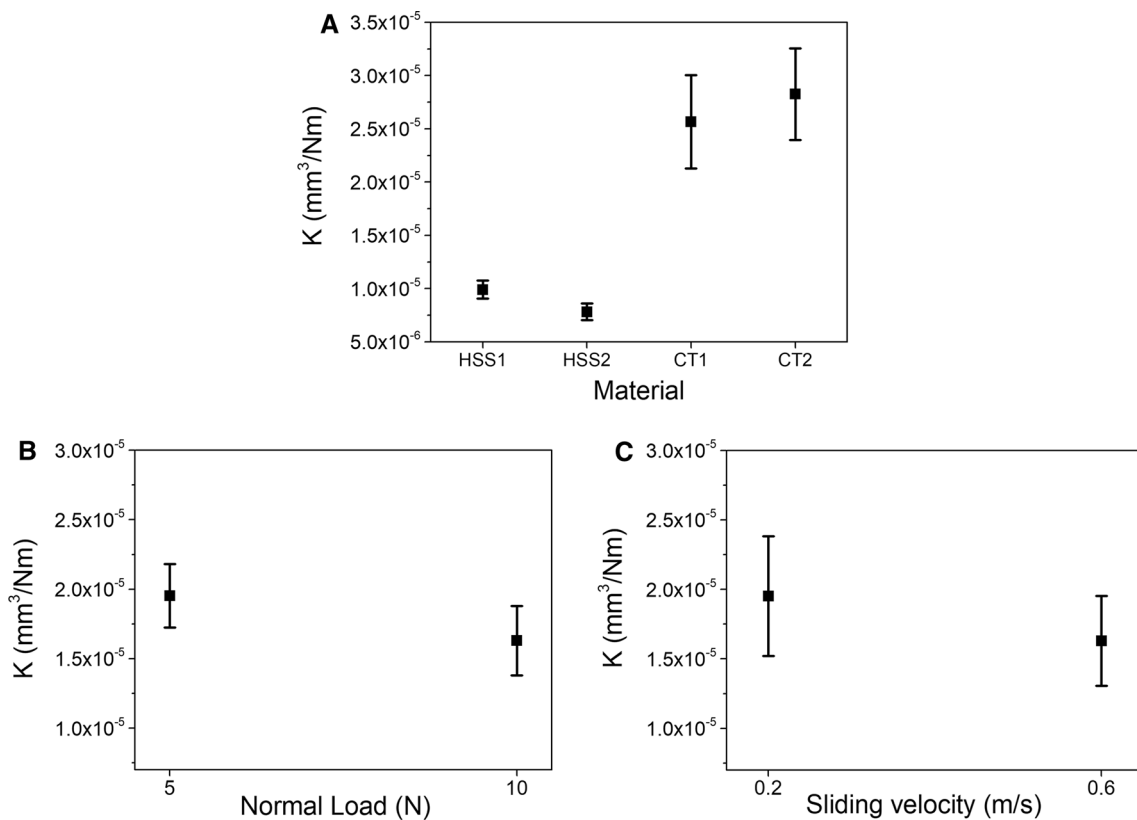


**Fig. 8** Wear coefficient  $k$  (mm<sup>3</sup>/Nm) as a function of **a** the alloy tested, **b** normal load and **c** sliding velocity

using the definition of the wear coefficient  $k$  (mm<sup>3</sup>/Nm) as is shown in Fig. 8. It is evident that large differences are present between the materials (Fig. 8a). An analysis of variance

(ANOVA) was performed to reveal the effect of each variable or factor, as well as its interactions on the wear response. The results show that statistically significant differences are

found between the materials tested, i.e., between HSS and Hi-Cr cast iron. However, it is not evident if appreciable differences exist between each treatment of the Hi-Cr cast iron or HSS materials themselves. Therefore, an additional Tukey test was performed to analyze the effect of the condition of the alloy on the wear response. The results showed that insignificant differences were observed between CT1 and CT2 and between HSS1 and HSS2. Therefore, insignificant differences were observed between the heat treatments in the alloys, possibly due to the significance of other factors, such as oxidative wear.

Interestingly, under the test conditions used, neither the normal load (Fig. 8b) nor the sliding velocity (Fig. 8b) showed any influence in the wear behavior, from the statistical point of view (corroborate by an ANOVA Analysis). The velocity effect and the normal load are not statistically significant, and the interactions between variables or factors do not affect the wear phenomenon. To the best author's knowledge, it is the first time that is reported that the normal load and the sliding velocity do not increase or decrease the wear rate. The explanation of this fact is because of this new approach of studding the wear phenomena of hot rolls materials using an oxidized counterbody. This counterbody has three main iron oxide layer, each one with a different hardness and lubricity behavior. It was found that the normal load or the velocity changes the contact conditions with the oxide layers as is shown schematically in the Fig. 9. As will be discussed in the next section, and in the wear surfaces section, this change in the contact of the pin's surface from a hard oxide layer to a soft oxide layer, not only decrease the wear rate, but also decrease the friction coefficients. This shows that the present counterbody represents more accurately the industrial tribological roll-oxide scale pair, facilitates the study of other phenomena that are not always present in the conventional roll-abrasive paper pair tests.

The reason for this is described by Archard's equation, which states that a low normal load corresponds to lower wear and a lower contact temperature for the pin-on-disc interface compared to higher normal loads [28, 29]. This produces higher oxidative wear and superficial softening of the substrate, favoring the detachment of the oxide. However, it is interesting to observe that despite similar macrohardness for the HSS and Hi-Cr, the wear behavior is different. The reasons for this will be discussed in Sect. 4.2 and include the fracture of  $M_7C_3$  carbides in the Hi-Cr, the lack of support of carbides in the matrix and different oxidative behavior of the carbides, which affect the oxide support.

#### 4.1 Friction Coefficients

The sliding velocity does not exhibit an effect on the friction coefficient. However, the effect of the normal load on the friction coefficient via the sliding distance for each material is shown in Fig. 10. At normal load of 5 N, the friction coefficient varied from  $\sim 0.71$  to  $\sim 0.98$ , whereas for a normal load of 10 N, the friction coefficient value varied from  $\sim 0.45$  to  $\sim 0.63$ . These seemingly counterintuitive results are mainly explained by the detachment and/or removal of the external oxide (which is mainly composed of hematite) from the counterbody (ASTM A36 oxidized steel) due to occasional contact with the pin's surface (evidence of this is reported in Sects. 4.2.1.1, 4.2.2.3). This implies that for a normal load of 10 N, the pin's surface starts to interact with the second layer of oxide in the counterbody, which was composed of magnetite [20] (see Sects. 4.2.1.1, 4.2.2.3). This oxide is well known to have a lower hardness and higher lubricity than hematite [20]. A further analysis of this behavior is described in greater detail in Sect. 4.2 and included an analysis of the counter body surfaces. However, a difference between the HSS and Hi-Cr cast iron is

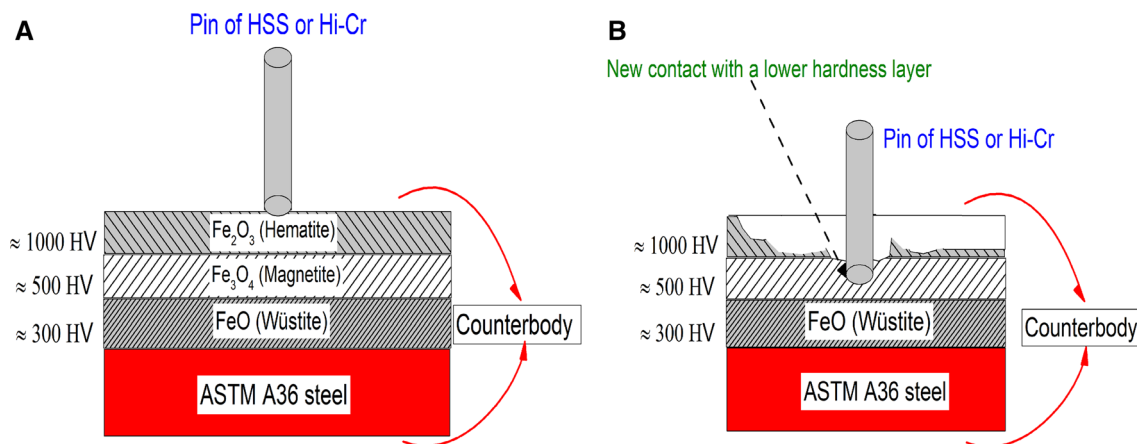


**Fig. 9** Schematic representation of the wear phenomenon at a **a** low normal load or low sliding velocity, and **b** high normal load and high sliding velocity



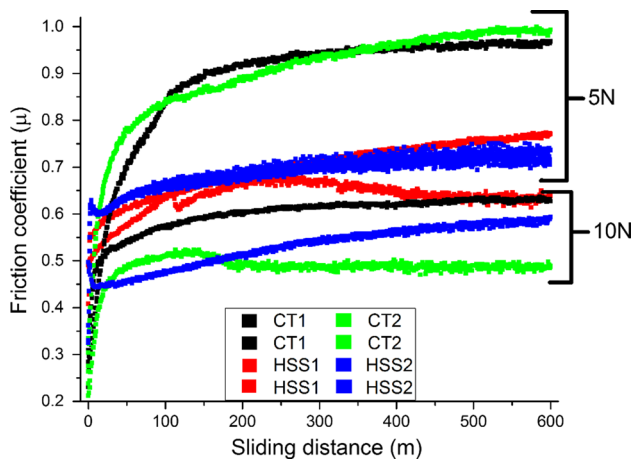


**Fig. 10** Friction coefficient as a function the sliding distance for various alloys. For interpretation lead the following example: the CT2 treatments were evaluated in two conditions; 5 and 10 N, for this reason in the graph appear two friction curves

easily recognized. For instance, both Hi-Cr cast iron alloys exhibited the highest change in friction coefficients during testing as a function of load, and the HSS alloys exhibited

intermediate values for both 5 and 10 N. The reason for this lies in the microstructure. Oxide formation occurs on the MC carbides in the HSS, which results in a lower friction coefficient, whereas for the Hi-Cr cast iron, there was no evidence of oxide formation on the carbides, which increases the friction coefficient.

## 4.2 Wear Surfaces

### 4.2.1 HSS

A stable oxide favors a reduction in the friction coefficient [6]. However, a non-stable and non-homogenous oxide is not supported by the matrix and favors the detachment of oxide particles. The oxide particles will generate abrasive wear due to their higher hardness, as shown in Fig. 11a. In Fig. 11b, c, oxidative wear is observed due to small oxide particles that have detached from the main body and result in abrasive wear effects, such as microcutting (see Fig. 11d) or microploughing in the matrix.

The oxides are formed primarily in the interface between the carbides and the matrix. The oxide continues to form on the matrix, which is more susceptible to oxidation than

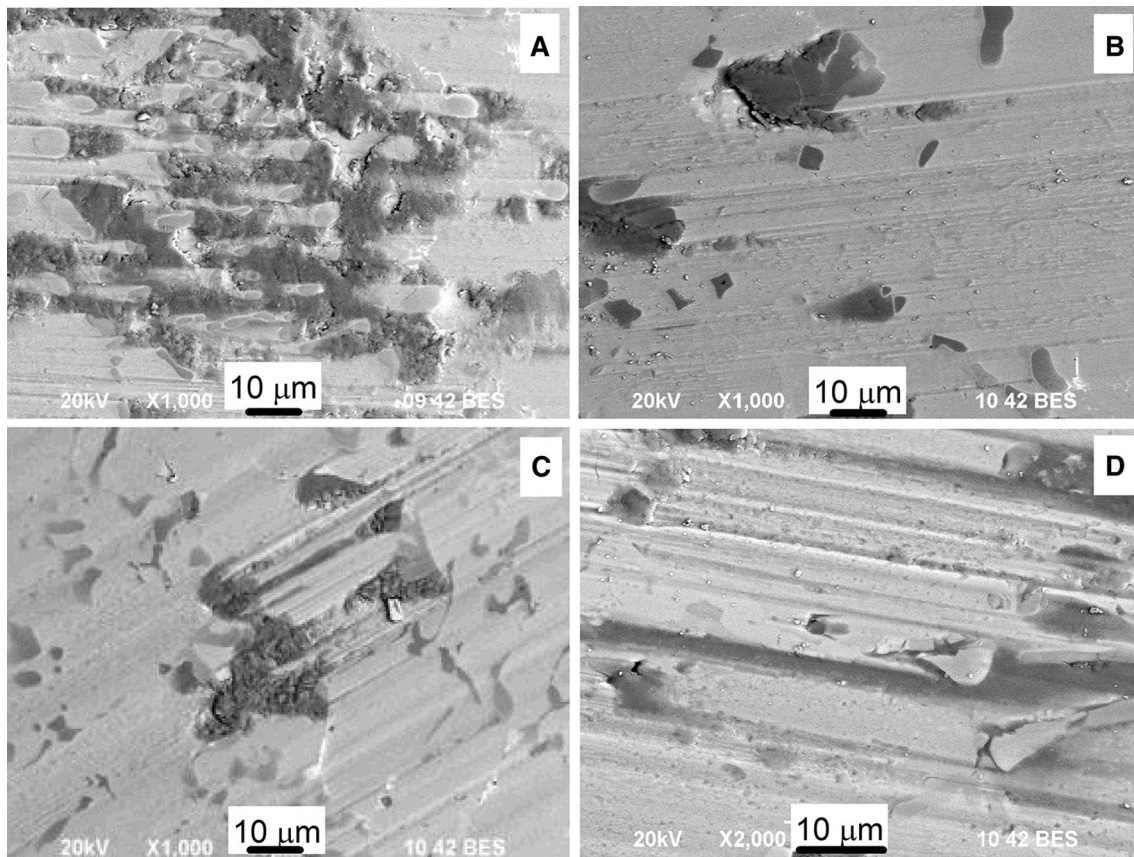


**Fig. 11** Features of the wear surfaces for all the HSS steels: **a** non-homogenous oxide, **b, c** detachment of oxide particles and **d** microcutting

the carbides. Figure 12a shows evidence of oxide locations (zone 1) around vanadium carbides (zone 2). Similar results were reported by Pellizzari et al. [2].

Zhu et al. [30] described that the  $M_7C_3$  and  $M_2C$  did not exhibit any signs of oxidation, resulting in no stable and homogeneous oxide layer formation on matrix. Meanwhile, the MC carbides exhibited severe oxidation due to the low thermal stability of the vanadium carbides, and the high energy at the interface carbide/matrix. These results were verified here using EDS (Table 6). Figure 12b shows oxides with a high oxygen content presented in zone 1. Zone 2 was determined to contain MC carbide due to the high vanadium content, and zone 3 was determined to be the matrix, due to its high iron content (this zone was free of any oxides).

**4.2.1.1 Counterbody Wear Surface (Against the HSS Pins)** The wear track on the oxidized ASTM A36 disc for the HSS is shown in Fig. 13. There are three main characteristic zones. The first zone (dark zones at bottom and top of the figure) is characterized by unfractured oxides. The second zone has a red color and is characterized by fracturing of the disc oxides and compacted wear debris. A third zone is identified by a gray color at the center of the image. This zone corresponds to a surface generated by oxide detach-

ment. A detailed observation of this zone performed via SEM is shown in Fig. 13b and reveals a dark zone corresponding to the pin contacting the counterbody (zone 1) and a zone (zone 2) with a brighter tone that is not affected by contact with the pin's surface.

Both zones (1 and 2) correspond to iron oxides. However, the EDS revealed that the contact zone (zone 1) contained less oxygen compared to the non-contact zone (zone 2), as shown in Table 7.

The chemical differences between these zones indicate the type of oxide involved. According to Ginzburg [31], hematite ( $Fe_2O_3$ ) has a high oxygen content of approximately 30% by weight, whereas the magnetite ( $Fe_3O_4$ ) reaches 28% oxygen by weight. In addition, the color differences between the zones revealed the type of the oxide. According to Liu et al. [32], the gray color is related to the presence of magnetite ( $Fe_3O_4$ ), whereas the red color is related to hematite ( $Fe_2O_3$ ). This reveals that the wear test performed here promotes the detachment of more external oxides (hematite) and facilitates pin contact with the inner oxides (magnetite layer). This explains the unstable friction coefficient curves and the decrease in the friction coefficient for high normal loads.

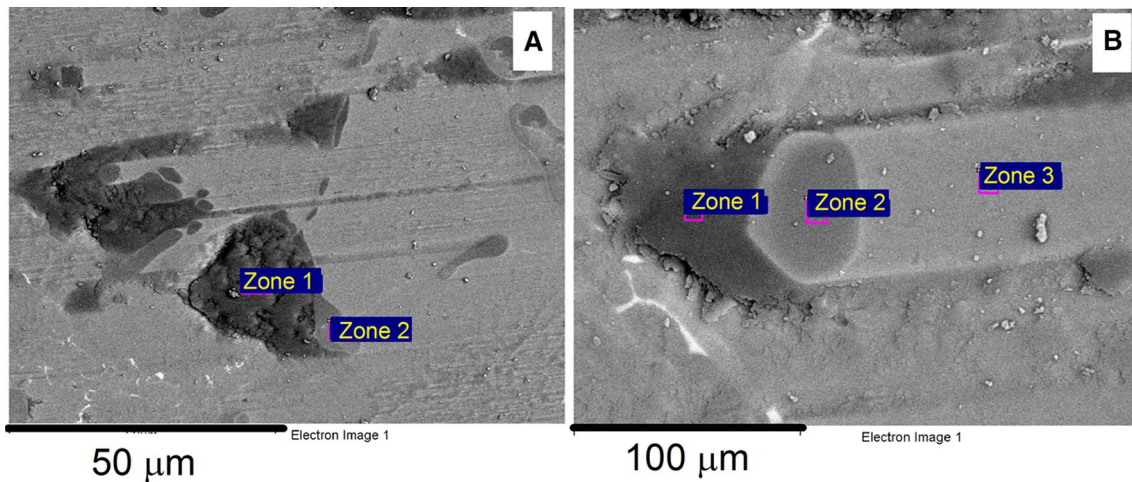


**Fig. 12** Wear surfaces and EDS results for the pins tested at 10 N and 0.6 m/s for **a** HSS1 and **b** HSS2

**Table 6** EDS results for the zones referenced in Fig. 12

| wt%        | C     | O     | Si   | S    | V     | Cr   | Fe    | Mo   | W     | Total |
|------------|-------|-------|------|------|-------|------|-------|------|-------|-------|
| Figure 12a |       |       |      |      |       |      |       |      |       |       |
| Zone 1     | 5.04  | 27.48 | –    | –    | 1.46  | 1.88 | 64.15 | –    | –     | 100   |
| Zone 2     | 12.50 | –     | –    | –    | 55.48 | 7.54 | 2.37  | 5.23 | 16.88 | 100   |
| Figure 12b |       |       |      |      |       |      |       |      |       |       |
| Zone 1     | 4.18  | 22.78 | –    | –    | 2.33  | 7.97 | 60.34 | –    | 2.40  | 100   |
| Zone 2     | 10.00 | –     | –    | 0.67 | 64.57 | 6.62 | 3.99  | –    | 14.16 | 100   |
| Zone 3     | 4.93  | –     | 0.79 | –    | 1.48  | 6.52 | 86.28 | –    | –     | 100   |

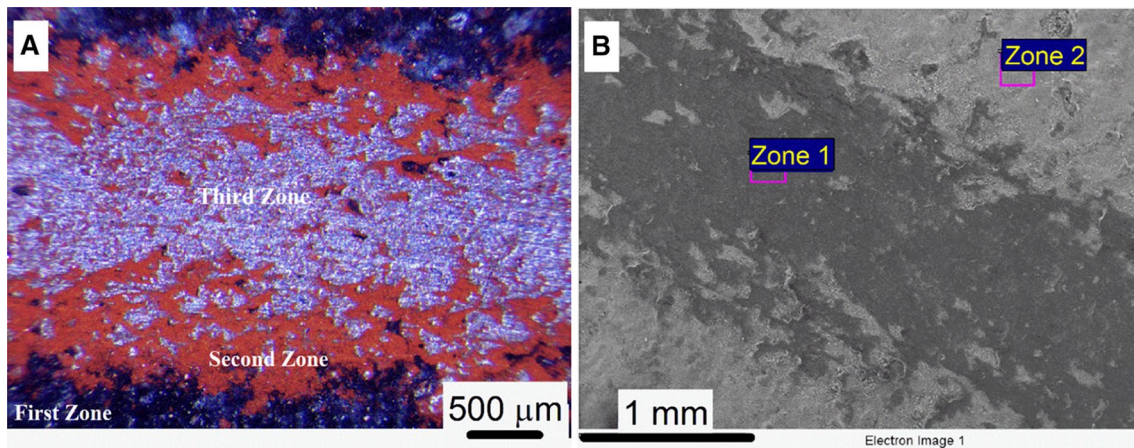


**Fig. 13** Wear surfaces of the ASTM A36 disc caused by the HSS2 pin at 10 N and 0.6 m/s observed via **a** optical microscopy and **b** SEM-EDS

**Table 7** EDS of the zones referenced in the Fig. 13

| wt%    | C     | O     | Fe    | Total |
|--------|-------|-------|-------|-------|
| Zone 1 | 6.40  | 30.01 | 63.58 | 100   |
| Zone 2 | 25.29 | 25.50 | 49.21 | 100   |

#### 4.2.2 Hi-Cr Cast Iron

**4.2.2.1 CT1** Figure 14a shows the wear surfaces of the pin tested at the lowest normal load and sliding velocity. Smooth wear depths and some fracture of the  $M_7C_3$  carbides are shown in Fig. 14a. Crack propagation occurs perpendicular to the carbide edge, and its further propagation is caused by a lack of carbide support in the matrix. The wear surfaces of the pin tested at the highest normal load and sliding velocity are shown in Fig. 14b. There is higher

oxidation of the matrix than is observed for the lowest test conditions. Figure 14b shows a deeper wear track and fragmentation of the carbides as a result of the abrasive, as well as higher oxidative wear in the matrix. The oxides form and accumulated around the primary carbides, which promotes mass loss around them and favors a lack of carbide support, causing further detachment and fracture. As shown in Fig. 15 and Table 8, the EDS results show that the oxides were formed from the matrix present on the pin's surface due to the high-chromium content and were not transferred from the oxidized disc.

**4.2.2.2 CT2** The wear surfaces for CT2 are shown in Fig. 16. Figure 16a shows the wear surface of the pin tested at the lowest normal load and sliding velocity with shallow grooves and only a few oxidation spots observed. Besides, that oxide formation and adherence is scarce. Additionally,

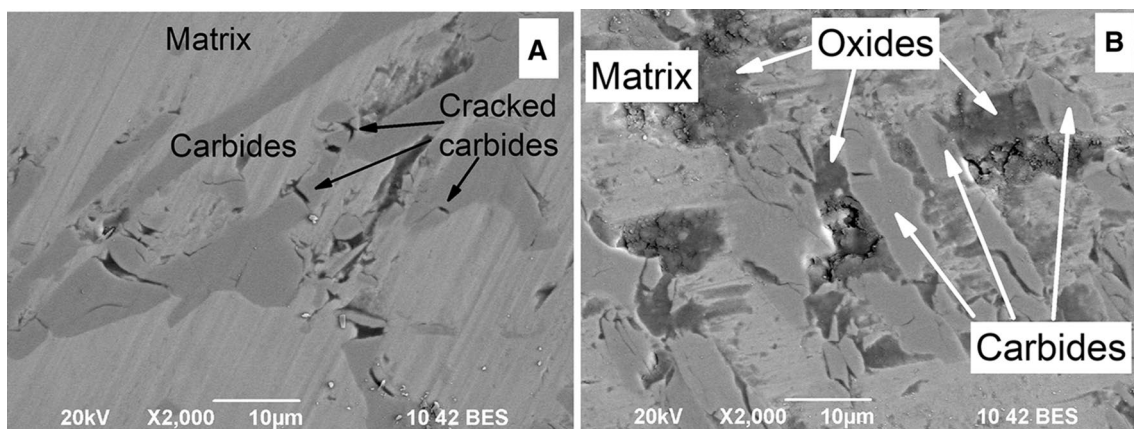


**Fig. 14** SEM of the wear surface for CT1: **a** 5 N and 0.2 m/s, and **b** 10 N and 0.6 m/s

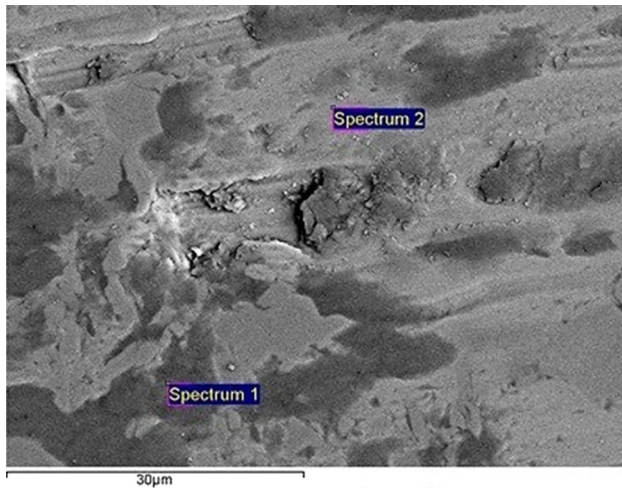


**Fig. 15** Wear surfaces and EDS results for a pin tested at 10 N and 0.6 m/s for the Hi-Cr cast iron at CT1

no evidence of carbide detachment or fracture was found under these conditions. The carbides observed correspond to  $M_2C$  carbides (secondary molybdenum carbides), which have a higher fracture resistance than the  $M_7C_3$  carbides [33]. The Fig. 16b shows the wear surfaces for the pin tested at the highest normal load and sliding velocity. Pronounced grooves in the matrix caused by abrasive wear are present.

However, the detachment of carbides and oxidative wear is negligible. This is because the martensitic matrix supports better the carbides than the austenitic matrix (or retained austenite in this case) [34], and because the secondary  $M_2C$  and  $M_{23}C_6$  carbides have good toughness, which increases the wear resistance [12, 35].

**4.2.2.3 Counterbody Wear Surface (Against the Hi-Cr Pins)** The wear track on the oxidized ASTM A36 disc for the Hi-Cr pin is shown in Fig. 17. Figure 17b shows the SEM image of the wear track observed in the optical microscope (Fig. 17a). The brightest zone corresponds to the wear track, and the darkest zone corresponds to the area not affected by the pin contact. In contrast to the results for the wear track with the HSS (see Sect. 4.2.1.1), here both zones (spectrum 1 and 2) are characterized by the presence of chromium oxides (Table 9). This means that oxides from the pin's surface were transferred to the oxidized ASTM A36 disc. This leads to inferring that Hi-Cr cast iron's oxides are less stable than the HSS's oxide. Due to the detachment corroborated of the first ones on the counterbody's surface, and this important phenomenon supports the observed higher wear of Hi-Cr cast iron than the HSS (see Sect. 4), in the evaluated conditions.

**Table 8** EDS results for the zones referenced in Fig. 15

| wt%        | C    | O     | Cr   | Mn   | Fe    | Ni   | Total |
|------------|------|-------|------|------|-------|------|-------|
| Spectrum 1 | 3.69 | 20.71 | 7.46 | –    | 68.15 | –    | 100   |
| Spectrum 2 | 3.36 | 1.58  | 9.79 | 1.55 | 82.08 | 1.63 | 100   |

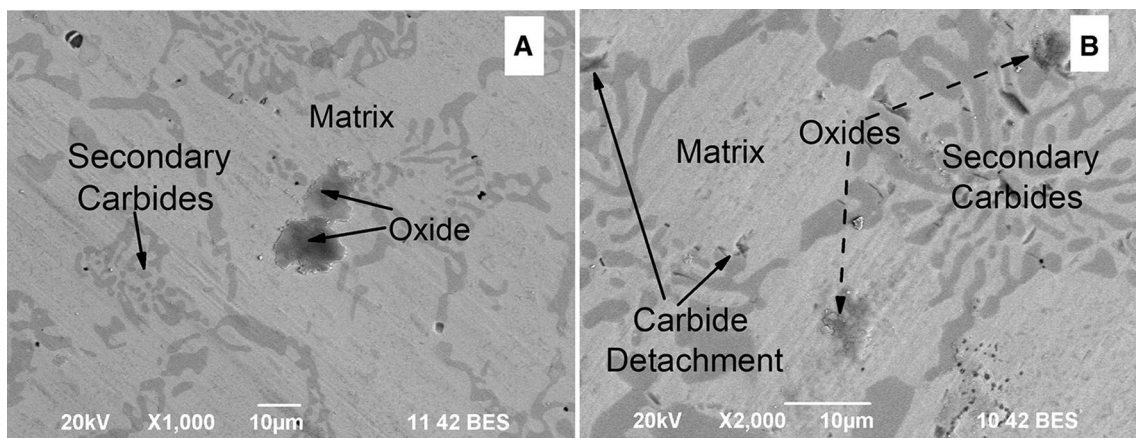


**Fig. 16** SEM images of the wear surface for CT2: **a, b** 5 N and 0.2 m/s and **c, d** 10 N and 0.6 m/s

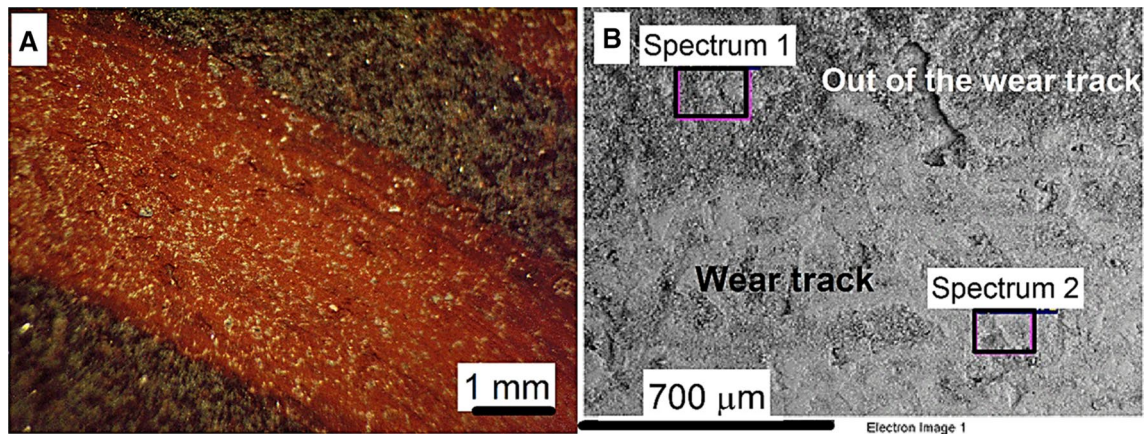


**Fig. 17** Wear surfaces of the ASTM A36 disc caused by the CT1 pin at 10 N and 0.6 m/s from **a** optical microscope and **b** SEM-EDS

**Table 9** EDS results for the zones referenced in Fig. 17

| wt%                   | C    | O     | Si   | Cr   | Fe    | Total |
|-----------------------|------|-------|------|------|-------|-------|
| Out of the wear track | 4.28 | 27.34 | 0.41 | –    | 67.97 | 100   |
| Wear track            | 5.03 | 28.85 | –    | 2.97 | 63.16 | 100   |

## 5 Conclusions

In this work, wear testing of Hi-Cr cast iron (subjected to cryogenic treatments) and HSS (subjected to tempering treatments) using an oxidized ASTM A36 disc was performed at two normal loads and two sliding velocities. The major conclusions from this work are summarized as follows:

- The oxide that formed at high temperatures (950 °C) over the surface of the ASTM A36 disc possesses good properties for use as a counterbody in the pin-on-disc configuration. In contrast to standard counterbodies, these oxides are a better approximation of the oxides that form during the hot rolling process.
- For all the tests conditions, the friction coefficient was directly related to the phenomena occurring in the counterbody oxides during the tests and its interactions with the normal load.
- The fracture of the  $M_7C_3$  carbides in the Hi-Cr cast iron and the different oxidative behavior of the carbides, which affect the oxide support, were responsible for the low wear resistance of the Hi-Cr cast iron compared to the HSS. Oxidative wear was the main wear mechanism in the conditions studied. No evidence of any oxide transferring from the pin's surface to the counterbody was observed for the HSS, but this was observed for the Hi-Cr cast iron.

- The oxides formed and accumulated in the interface between the matrix and the vanadium carbides. The oxide particles from the counterbody or the oxide pin's surface caused wear on the HSS matrix via microcutting and microploughing wear micro-mechanisms. A matrix with a more homogeneous oxide layer surrounding the MC carbides was shown to be less susceptible to cutting by the oxide particles.

**Acknowledgements** The authors would like to acknowledge the support of the Universidad del Valle (Colombia) for the Bolsa Concurable 2017.

## References

1. Pellizzari, M., Cescato, D., De Flora, M.G.: Hot friction and wear behaviour of high speed steel and high chromium iron for rolls. *Wear* **267**, 467–475 (2009)
2. Pellizzari, M., Molinari, A., Straffellini, G.: Tribological behaviour of hot rolling rolls. *Wear* **259**, 1281–1289 (2005)
3. Milan, J.C.G., Carvalho, M.A., Xavier, P.R., Franco, S.D., De Mello, J.D.B.: Effect of temperature, normal load and pre-oxidation on the sliding wear of multi-component ferrous alloys. *Wear* **259**, 412–423 (2005)
4. Coronado, J.J., Sinatora, A.: Load effect in abrasive wear mechanism of cast iron with graphite and cementite. *Wear* **267**, 6–11 (2009)
5. Coronado, J.J., Gomez, A., Sinatora, A.: Tempering temperature effects on abrasive wear of mottled cast iron. *Wear* **267**, 2070–2076 (2009)

6. Zambrano, O.A., Coronado, J.J., Rodríguez, S.A.: Tempering temperature effect on sliding wear at high temperatures in mottled cast iron. *Tribol. Lett.* **57**, 1–11 (2015)
7. Coronado, J.J.: Effect of load and carbide orientation on abrasive wear resistance of white cast iron. *Wear* **270**, 823–827 (2011)
8. Penagos, J.J., Ono, F., Albertin, E., Sinatora, A.: Structure refinement effect on two and three-body abrasion resistance of high chromium cast irons. *Wear* **340**, 19–24 (2015)
9. Joos, O., Boher, C., Vergne, C., Gaspard, C., Nylen, T., Rezai-Aria, F.: Assessment of oxide scales influence on wear damage of HSM work rolls. *Wear* **263**, 198–206 (2007)
10. Munther, P.A., Lenard, J.G.: The effect of scaling on interfacial friction in hot rolling of steels. *J. Mater. Process. Technol.* **88**, 105–113 (1999)
11. Fernandez-Pariente, I., Belzunce, F.J.: Wear and oxidation behaviour of high-chromium white cast irons. *Mater. Charact.* **59**, 669–674 (2008)
12. Doğan, Ö.N., Hawk, J.A., Laird, G.: Solidification structure and abrasion resistance of high chromium white irons. *Metall. Mater. Trans. A* **28**, 1315–1328 (1997)
13. Tabrett, C., Sare, I.: Effect of high temperature and sub-ambient treatments on the matrix structure and abrasion resistance of a high-chromium white iron. *Scripta Mater.* **38**, 1747–1753 (1998)
14. Liu, H.H., Wang, J., Yang, H.S., Shen, B.L.: Effects of cryogenic treatment on microstructure and abrasion resistance of CrMnB high-chromium cast iron subjected to sub-critical treatment. *Mater. Sci. Eng., A* **478**, 324–328 (2008)
15. Xavier, R.R., de Carvalho, M.A., Cannizza, E., White, T.H., Rivaroli, A., Sinatora, A.: Development and application of high speed steel rolls for long products. In: 45th MWSP Conference Proceedings ISS-AIME, p. 121 (2003)
16. Xavier, R.R., de Carvalho, M.A., Cannizza, E., Kerr, E.J., Silva, C.S.: Successful strategy for HSS rolls implementation. *Mater. Sci. Technol. Assoc. Iron Steel Technol.* **4**, 2 (2005)
17. Park, J.W., Lee, H.C., Lee, S.: Composition, microstructure, hardness, and wear properties of high-speed steel rolls. *Metall. Mater. Trans. A* **30**, 399–409 (1999)
18. Vitry, V., Nardone, S., Breyer, J.P., Sinnaeve, M., Delaunois, F.: Microstructure of two centrifugal cast high speed steels for hot strip mills applications. *Mater. Des.* **34**, 372–378 (2012)
19. Nilsson, M., Olsson, M.: Microstructural, mechanical and tribological characterisation of roll materials for the finishing stands of the hot strip mill for steel rolling. *Wear* **307**, 209–217 (2013)
20. Zambrano, O.A., Coronado, J.J., Rodríguez, S.A.: Mechanical properties and phases determination of low carbon steel oxide scales formed at 1200 C in air. *Surf. Coat. Technol.* **282**, 155–162 (2015)
21. Rietveld, H.M.: A profile refinement method for nuclear and magnetic structures. *J. Appl. Crystallogr.* **2**, 65–71 (1969)
22. Larsen, A., Von Dreele, R.: GSAS, General structure analysis system. LANSCE, MS-H805, Los Alamos National Laboratory, Los Alamos (1994)
23. Silva, W.S.D.: Estudo da tenacidade à fratura do aço rápido M2 fundido, modificado e tratado termicamente. Universidade de São Paulo. <http://goo.gl/angUcW> (2001)
24. Firouzdor, V., Nejati, E., Khomamizadeh, F.: Effect of deep cryogenic treatment on wear resistance and tool life of M2 HSS drill. *J. Mater. Process. Technol.* **206**, 467–472 (2008)
25. Molinari, A., Pellizzari, M., Biggi, A., Corbo, G., Tremea, A.: Primary carbides in spincast HSS for hot rolls and their effect on the oxidation behaviour. In: Proceedings of the 6th tooling conference, Sweden, pp. 437–452 (2002)
26. Wang, J., Xiong, J., Fan, H.Y., Yang, H.S., Liu, H.H., Shen, B.L.: Effects of high temperature and cryogenic treatment on the microstructure and abrasion resistance of a high chromium cast iron. *J. Mater. Process. Technol.* **209**, 3236–3240 (2009)
27. Nilsson, M., Microstructural, M.O.: mechanical and tribological characterisation of roll materials for the finishing stands of the hot strip mill for steel rolling. *Wear* **307**, 209–217 (2013)
28. So, H.: The mechanism of oxidational wear. *Wear* **184**, 161–167 (1995)
29. Quinn, T.F.J.: The oxidational wear of low alloy steels. *Tribol. Int.* **35**, 691–715 (2002)
30. Zhu, Q., Zhu, H.T., Tieu, A.K., Kong, C.: Three dimensional microstructure study of oxide scale formed on a high-speed steel by means of SEM, FIB and TEM. *Corros. Sci.* **53**, 3603–3611 (2011)
31. Ginzburg, V.B.: Steel-rolling technology: theory and practice. Marcel Dekker, Inc, New York (1989)
32. Liu, S., Tang, D., Wu, H.B., Wang, L.D.: Oxide scales characterization of micro-alloyed steel at high temperature. *J. Mater. Process. Technol.* **213**, 1068–1075 (2013)
33. Ji, Y.P., Wu, S.J., Xu, L.J., Li, Y., Wei, S.Z.: Effect of carbon contents on dry sliding wear behavior of high vanadium high speed steel. *Wear* **294**, 239–245 (2012)
34. Coronado, J.J., Sinatora, A.: Abrasive wear study of white cast iron with different solidification rates. *Wear* **267**, 2116–2121 (2009)
35. Sare, I.R.: Abrasion resistance and fracture toughness of white cast irons. *Metals Technol.* **6**, 412–419 (2013)